Study of the vortex shedding flow around a body near a moving ground

Alex Mendonça Bimbato [a,*], Luiz Antonio Alcântara Pereira [a], Miguel Hiroo Hirata [b]

[a] Institute of Mechanical Engineering, Federal University of Itajuba, Itajuba, CP 50, Minas Gerais, Brazil
[b] State University of Rio de Janeiro, FAT-UERJ, Resende, Rio de Janeiro, Brazil

ARTICLE INFO

ABSTRACT

The two-dimensional viscous incompressible fluid flow around a circular cylinder near a moving ground is numerically simulated. In a moving ground one eliminates the influence of the ground boundary layer, which is a crucial factor in the numerical simulation of the flow around a body moving in a close vicinity to a flat ground. A Lagrangian mesh-free vortex method is used to calculate global and local quantities of high Reynolds number flow of 1.0×10^5. This method is modified to take into account the sub-grid scale phenomena through a second-order velocity structure function model adapted to the Lagrangian scheme. In the present algorithm vortices with a Lamb core are generated only on the circular cylinder surface to ensure that the no-slip condition is satisfied and that the circulation is conserved. On the ground it is only sufficient to ensure the impermeability condition. Based on the experimental results available in the literature, the critical drag behaviour was found to be directly related to a global change in the near wake structure of the cylinder.

1. Introduction

The aerodynamic loads acting on bluff bodies are induced by complex flow fields and are of scientific importance in engineering problems. A number of applications can be found in mechanical, civil and naval engineering that employ circular–cylindrical structures, such as tall buildings, bridge piers, chimneys, periscopes, heat exchangers tubes, cables, wires, and so on.

In scientific terms, the flow around circular cylinders includes a variety of fluid dynamics phenomena, such as separation, vortex shedding and the transition to turbulence. The mechanisms of vortex shedding and its suppression have significant effects on the various fluid-mechanical properties of practical interest such as flow-induced forces, vibrations and noises and the efficiencies of heat and mass transfer. For a better and easy understanding of the physics, therefore, it is reasonable to focus our attention on the flow around bodies of simple geometry such as a circular cylinder. Cylinders having a two-dimensional structure are very suitable for restricting the complexity and thus observing the fundamental features of the flow.

The fluid flow around a circular cylinder close to a plane wall is influenced not only by the Reynolds number but also by the gap between the cylinder and the ground, h, characterized by the gap ratio h/d (d is the cylinder diameter). The fundamental effects of gap ratio have been successfully observed by Taneda (1965), Roshko et al. (1975), Bearman and Zdravkovich (1978), Grass et al. (1984), Zdravkovich (1985a), Lei et al. (1999) and Lin et al. (2005).

As the gap ratio becomes smaller the influence of the ground boundary layer becomes important and the mechanisms resulting from its interaction with the body boundary is still unclear despite several intensive studies reported so far. Roshko et al. (1975) measured the time-averaged drag and lift coefficients, C_D and C_L, for a circular cylinder placed near a fixed wall in a wind tunnel at $Re = 2.0 \times 10^4$, which lies in the upper-subcritical flow regime; they showed that the C_D rapidly decreased and C_L increased as the cylinder came close to the wall. Zdravkovich (1985b) measured the time-averaged drag force for a circular cylinder at $4.8 \times 10^4 < Re < 3.0 \times 10^5$ and reported that the rapid decrease in drag occurred as the gap was reduced to less than the thickness of the boundary layer δ/d on the ground, and concluded that the variation of C_D was dominated by h/δ rather than by the conventional gap ratio h/d. He also noted that the C_L could be significantly affected by the state of the boundary layer, although it was insensitive to the thickness of the boundary layer.

Zdravkovich (2003) reported the drag behaviour for a circular cylinder placed near a moving ground running at the same speed as the freestream for high Reynolds number of 2.5×10^5, which lies within the critical flow regime rather than the subcritical flow regime. The experiment made by Zdravkovich (2003) showed some differences to all the above studies. First, practically no boundary layer developed on the ground. Second, the decrease in drag due to the decrease in h/d did not occur in the measurements. The differences encountered were attributed to the non-existence of the wall boundary layer or the high Reynolds number.

In a recent work, Nishino (2007) presented experimental results of a circular cylinder with an aspect ratio of 8.33, with and without end-plates, placed near and parallel to a ground running at the same speed as the freestream, where substantially no boundary

* Corresponding author. Tel.: +5535 3629 1299; Fax: +5535 3629 1148
E-mail address: alexbimbato@unifei.edu.br (A.M. Bimbato).

layer develops to interfere with the cylinder. Measurements were carried out at two upper-subcritical Reynolds numbers of 0.4×10^5 and 1.0×10^5. The results produced new insights into the physics of the phenomenon. According to the experiments for the cylinder with end-plates, on which the oil flow patterns were observed to be essentially two dimensional, the drag rapidly decreases as h/d decreases to less than 0.5 but becomes constant for h/d less than 0.35, unlike the usually obtained results with a fixed ground.

Due to difficulties in measuring details of the time depending fluid flow, the utilization of numerical simulations could be a powerful tool to be used in this kind of analysis.

This paper describes a mesh-free method used to calculate global and local quantities of high Reynolds number flow around a circular cylinder located near a moving ground. The two-dimensional aerodynamic characteristics are investigated at a Reynolds number of 1.0×10^5 using turbulence modeling, which employs a second-order velocity structure function of the filtered field (Alcântara Pereira et al., 2002). The vortex method with turbulence modeling is used to analyze the influence of the moving ground running at the same speed as the freestream on the flow and force characteristics. Therefore comparisons are made with experimental results presented by Nishino (2007).

Vortex methods have been developed and applied for analysis of complex, unsteady and vortical flows, because they consist of simple algorithm based on physics of flow (Kamemoto, 2004). Vortex cloud modeling offers great potential for numerical analysis of important problems in fluid mechanics. With the Lagrangian formulation (e.g. Chorin ,1973; Leonard, 1980; Sarpkaya, 1989; Alcântara Pereira et al., 2004; Stock, 2007) a grid for the spatial discretization of the fluid region is not necessary. In addition, with the vortex method the attention is only directed to the regions of high activities, which are the regions containing vorticity; on the contrary, Eulerian schemes consider the entire fluid domain independent of the fact that there are sub-regions where less important, if any, flow activity can be found. Finally with the Lagrangian tracking of the vortices, one does not need to consider the far away boundary conditions. This is of importance in the wake region (which is not negligible in the flows of present interest) where turbulence activities are intense and unknown, a priori.

2. Governing equations and vorticity dynamics

Consider the flow around a circular cylinder immersed in a large fluid region bounded by a moving plane surface as shown in Fig. 1. A uniform incoming flow with freestream velocity U from left to right is assumed, where the coordinates system is fixed on the cylinder. The fluid is Newtonian with constant properties and flowing in a two-dimensional plane; the compressibility effects are neglected. Fig. 1 shows the domain Ω with boundary $S = S_1 \cup S_2 \cup S_\infty$, S_1 being the body surface, S_2 the moving plane running at the same speed as the incident flow and S_∞ the far away boundary.

Due to the no-slip condition, a shear flow is set on the cylinder surface and, as a consequence, vorticity is generated. The vorticity

that develops in the body boundary layer is carried downstream into the viscous wake; further developments of this wake will be influenced by the presence of the nearby moving ground.

As there is no shear flow on the surface of the moving ground, no vorticity is generated as already mentioned. However, it is worth to mention the necessity of imposing the impermeability condition on this surface.

The fluid flow is governed by the continuity and the Navier–Stokes equations, which can be written in the form:

$$\frac{\partial \overline{u}_i}{\partial x_i} = 0, \tag{1}$$

$$\frac{\partial \overline{u}_i}{\partial t} + \overline{u}_j \frac{\partial \overline{u}_i}{\partial x_j} = -\frac{1}{\rho}\frac{\partial \overline{p}}{\partial x_i} + 2\frac{\partial}{\partial x_j}\left[(\upsilon + \upsilon_t)\overline{S}_{ij}\right], \tag{2}$$

where the summation convention applies. The above governing equations were filtered ($u_i = \overline{u}_i + u'_i$, u'_i denotes the fluctuation field), υ is the fluid kinematics viscosity coefficient, υ_t is the eddy viscosity coefficient, ρ is the fluid density, $\overline{S}_{ij}$ is the deformation tensor of the filtered field and p is the pressure.

The large structures are governed by Eq. (2) and the eddy-viscosity assumption (Boussinesq's hypothesis) is used to model the sub grid scale tensor $T_{ij} = -2\upsilon_t \overline{S}_{ij}$ (Smagorinsky, 1963).

The impermeability condition on the cylinder and ground surfaces is given by

$$u_n = v_n, \quad at \ S_1 \ and \ S_2, \tag{3}$$

where $v_n = 0$ is the normal component of the surface velocities.

The no-slip condition is imposed only on the cylinder surface

$$u_\tau = v_\tau, \quad at \ S_1, \tag{4}$$

where v_τ is the tangential component of the surface velocities. On the cylinder surface $v_\tau = 0$ and on the moving ground $v_\tau = U$.

One assumes that, far away, the perturbation caused by the body and moving ground fades as

$$|\mathbf{u}| \to U, \quad at \ S_\infty. \tag{5}$$

In order to take into account the local activity of turbulence, Métais and Lesieur (1992) considered that the small scales may not be too far from isotropy and proposed to use the local kinetic-energy spectrum $E_{(kc)}$ at the cut-off wave number (k_c) to define the eddy viscosity υ_t. Using a relation proposed by Batchelor (1953) the local spectrum at k_c is calculated with a local second-order velocity structure function $\overline{F}_2$ of the filtered field (Lesieur and Métais, 1996):

$$\overline{F}_2(\mathbf{x}, \varDelta, t) = \overline{\left\| \overline{\mathbf{u}}(\mathbf{x},t) - \overline{\mathbf{u}}(\mathbf{x}+\mathbf{r},t) \right\|^2}_{\|\mathbf{r}\| \, = \, \varDelta}. \tag{6}$$

where the velocities $\overline{\mathbf{u}}(\mathbf{x}+\mathbf{r})$ are calculated over the surface of a sphere of radius $\varDelta$.

From the Kolmogorov spectrum the eddy viscosity can be written as a function of $\overline{F}_2$:

$$\upsilon_t(\mathbf{x}, \varDelta, t) = 0.105 C_k^{-(3/2)} \varDelta \sqrt{\overline{F}_2(\mathbf{x}, \varDelta, t)}, \tag{7}$$

where $C_k = 1.4$ is the Kolmogorov constant. The great computational advantage of this formulation over the Smagorinsky (1963)
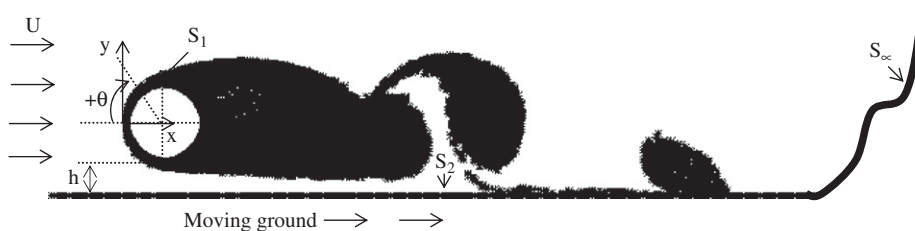

Fig. 1. Flow around a circular cylinder near a moving ground.

model is that in Eq. (6) the notion of velocity fluctuations (differences of velocity) is used instead of the rate of deformation (derivatives).

Alcântara Pereira et al. (2002) adapted the definition of the second-order velocity structure function $\overline{F}_2$ to the Lagrangian scheme in 2-D as

$$\overline{F}_2 = \frac{1}{NV} \sum_{l=1}^{NV} \|\mathbf{u}(\mathbf{x}) - \mathbf{u}(\mathbf{x}+r_1)\|_l^2 \left(\frac{\sigma_{0v_t}}{\|r_l\|}\right)^{(2/3)}. \tag{8}$$

In Eq. (8), NV is the number of discrete vortices of the cloud found in the region defined by the distances $r_1 = 0.1\sigma$ and $r_2 = 2.0\sigma$ from the centre of each vortex particle, where σ is the core radius of a Lamb vortex (Eq. 16), which is used as a model for the discrete vortices of the cloud. A correction $(\sigma_{0v_t}/\|r_l\|)^{2/3}$ is necessary due to the fact that the NV vortices are not located at equal distance from the centre of each investigated vortex particle.

$\overline{F}_2$ represents a local statistical average of square velocity differences between free vortices located in the region defined by the distances $r_1 = 0.1\sigma$ and $r_2 = 2.0\sigma$ from the centre of each vortex particle. Physically, this function represents the flow fluctuation (turbulent activities) in the neighborhood of the vortex located at x.

The Reynolds number is defined as

$$\mathrm{Re} = \frac{Ud}{v}, \tag{9}$$

where d is the cylinder diameter. The dynamics of the fluid motion, governed by the boundary-value problems (1)–(5) can be alternatively studied by taking the curl of Eq. (2), obtaining the new 2-D vorticity transport equation:

$$\frac{\partial \omega}{\partial t} + \mathbf{u} \cdot \nabla \omega = \frac{1+v_t^*}{Re} \nabla^2 \omega, \tag{10}$$

in which ω is the only non-zero component of the vorticity vector and

$$v_t^* = \frac{v_t}{v}. \tag{11}$$

3. The discrete vortex method with turbulence model

3.1. Discrete vortex method (large scale simulation)

The vortex method proceeds by representing the continuous vorticity field by a cloud of elemental vortices; each vortex is characterized by a vorticity distribution, $\varsigma_{\sigma i}$ (the cut-off function), a circulation strength Γ_i, a core size σ_i and its location x_i. Thus, the vorticity field is expressed by

$$\boldsymbol{\omega}(\mathbf{x},t) \approx \boldsymbol{\omega}^h(\mathbf{x},t) = \sum_{i=1}^{Z} \Gamma_i(t) \varsigma_{\sigma_i}(x - \mathbf{x}_i(t)). \tag{12}$$

where Z is the number of point vortices of the cloud used to simulate the vorticity field.

In this paper, the vorticity diffusion is simulated using the random walk method, so it is assumed that the core sizes are uniform($\sigma_i = \sigma$), and it is used the Gaussian distribution as the cut-off function; this choice of the cut-off function leads to the Lamb vortex (Leonard, 1980); thus

$$\varsigma_\sigma(\mathbf{x}) = \frac{1}{\pi\sigma^2} exp\left(-\frac{|\mathbf{x}|^2}{\sigma^2}\right). \tag{13}$$

The random walk method was introduced by Chorin (1973) and is formulated essentially as a fractional method. An integral form solution to the random walk problem is given by

$$\omega(x,t) = \int_{-\infty}^{\infty} (G(x,y,t) - G(x-y,t))f(y)dy, \tag{14}$$

where

$$G(x,y,t) = \frac{1}{\sqrt{4\pi((1+v_t^*)/\mathrm{Re})t}} e^{-(x-y)^2/4((1+v_t^*)/\mathrm{Re})t} \text{ and } v_t^* = 0. \tag{15}$$

However, when using the above described random walk scheme one departs from the Navier–Stokes equations which, in some sense, imply a "laminar diffusion process". In this context the core sizes are not changed. In the present paper the core sizes are evaluated locally, only where the flow is turbulent, which means a "turbulent diffusion of vorticity".

The value of the velocity structure function, which measures the turbulent manifestations, is statistically sound only if the neighborhood of each vortex particle is sufficiently populated with other vortex particles. If v_t^* is not zero, the turbulent activities are evaluated and the core sizes are modified under the following formula:

$$\sigma_{0v_t} = 4.48364\sqrt{\frac{\Delta t(1+v_t^*)}{\mathrm{Re}}}. \tag{16}$$

The expression proposed by Mustto et al. (1998) is obtained when $v_t^* = 0$ in Eq. (16).

The vorticity transport is simulated numerically by convecting the particles with the local fluid velocity and using a random walk displacement $\chi_j \equiv (\chi_{1j}, \chi_{2j})$ to account for the diffusion (molecular and turbulent) effects. The convection of each vortex particle (j) is governed by the equation:

$$\frac{d\mathbf{x}_j}{dt} = \mathbf{u}(\mathbf{x}_j, t), \tag{17}$$

and, according to the random walk method (Alcântara Pereira et al., 2002) the diffusive displacement of each vortex particle (j) is given by

$$\chi_j \equiv (\chi_{1j}, \chi_{2j}) = \sqrt{\frac{4\Delta t(1+v_t^*)}{\mathrm{Re}} \ln\left(\frac{1}{P}\right)} [\cos(2\pi Q) + i\sin(2\pi Q)],$$
$$j = 1, Z, \tag{18}$$

where $i = \sqrt{-1}$; P and Q are random numbers between 0.0 and 1.0.

The velocity field $\mathbf{u}(\mathbf{x},t)$ can be split into three parts (Hirata et al., 2008):

$$\mathbf{u}(\mathbf{x},t) = \mathrm{ui}(\mathbf{x},t) + \mathrm{ub}(\mathbf{x},t) + \mathrm{uv}(\mathbf{x},t). \tag{19}$$

The contribution of the incident flow is represented by $\mathbf{ui}(\mathbf{x},t)$ in Eq. (19). For a uniform oncoming flow its components take the form:

$$\mathbf{ui}_1 = 1 \text{ and } \mathbf{ui}_2 = 0. \tag{20}$$

The body and moving ground contribute to $\mathbf{ub}(\mathbf{x},t)$ in Eq. (19), which can be obtained, for example, using the boundary element method (Katz and Plotkin, 1991). The two components can be written as

$$\mathbf{ub}_i(x_j,t) = \sum_{k=1}^{NP} \psi_k c_{jk}^i(x_j(t) - x_k), \quad i = 1,2 \text{ and } j = 1,Z, \tag{21}$$

where NP is the total number of source flat panels representing the body and moving ground. It is assumed that the source strength per length is constant such that $\psi_k = $const. and $c_{jk}^i(x_j(t) - x_k)$ is the i component of the velocity induced at vortex j by a unit strength source flat panel located at k.

The velocity $\mathbf{uv}(\mathbf{x},t)$ due to the vortex interactions is obtained from the vorticity field by means of the Biot–Savart law:

$$\mathrm{uv}(\mathbf{x},t) = \int (\nabla \times \mathbf{G})(\mathbf{x}-\mathbf{x}')\boldsymbol{\omega}(\mathbf{x}',t)d\mathbf{x}'$$
$$= \int K(x-\mathbf{x}')\boldsymbol{\omega}(\mathbf{x}',t)d\mathbf{x}' = (\mathbf{K}*\boldsymbol{\omega})(\mathbf{x},t) \tag{22}$$

where $\mathbf{K} = \nabla \times \mathbf{G}$ is the Biot–Savart kernel, G is the Green's function for the Poisson equation and $*$ represents the convolution

operation. In two dimensions the Biot–Savart law is written explicitly as

$$uv(\mathbf{x},t) = \frac{-1}{2\pi} \int \frac{(x-x') \times \omega(\mathbf{x}',t)}{|x-x'|^2}. \tag{23}$$

The two components of Eq. (23) can be written as

$$uv_i(x_j,t) = \sum_{k=1}^{Z} \Gamma_k c_{jk}^i(x_j(t)-x_k(t)), \quad i=1,2 \text{ and } j=1,Z, \tag{24}$$

where Γ_k is the k-vortex strength and $c_{jk}^i(x_j(t)-x_k(t))$ is the i component of the velocity induced at vortex j by a unit strength vortex located at k.

The pressure calculation starts with the Bernoulli function, defined by Uhlman (1992) as

$$\overline{Y} = \frac{p}{\rho} + \frac{u^2}{2}, \quad u = |\mathbf{u}|. \tag{25}$$

Kamemoto (1993) used the same function and starting from the Navier–Stokes equations was able to write a Poisson equation for the pressure. This equation was solved using a finite difference scheme. Here the same Poisson equation was derived and its solution was obtained through the following integral formulation (Shintani and Akamatsu, 1994):

$$H\overline{Y}_i - \int_S \overline{Y}\nabla\Xi_i \cdot \mathbf{e}_n dS = \iint_\Omega \nabla\Xi_i \cdot (\mathbf{u} \times \boldsymbol{\omega})d\Omega - \frac{1}{\text{Re}} \int_S (\nabla\Xi_i \times \boldsymbol{\omega}) \cdot \mathbf{e}_n dS, \tag{26}$$

where $H=1$ in the fluid domain, $H=0.5$ on the boundaries, Ξ is a fundamental solution of the Laplace equation and e_n is the unit vector normal to the solid surfaces.

The drag and lift coefficients are expressed by

$$C_D = -\sum_{k=1}^{NP} 2(p_k-p_\infty)\Delta S_k \sin\beta_k = -\sum_{k=1}^{NP} C_P\Delta S_k \sin\beta_k \tag{27}$$

$$C_L = -\sum_{k=1}^{NP} 2(p_k-p_\infty)\Delta S_k \cos\beta_k = -\sum_{k=1}^{NP} C_P\Delta S_k \cos\beta_k, \tag{28}$$

where ΔS_k is the length and β_k is the angle of both the kth-panel.

3.2. Turbulence modeling (micro-scale simulation)

The concept of eddy viscosity, υ_t, as defined by Eq. (7), has to be considered in order to take into consideration the micro-scale manifestations of the turbulence.

In the numerical simulation, consider a discrete vortex of the cloud, which is located at point L. The value of the velocity structure function $\overline{F}_2$, which measures the turbulence manifestations, is statistically sound only if the neighborhood of L is sufficiently populated with other point vortices. It is sufficient to assume that this happens if $(NV/A) \geq 5000$, where NV is the number of point vortices in the region of area A, defined by two circumferences centred in L and with radius $r_1=0.1\sigma$ and $r_2=2.0\sigma$ (Alcântara Pereira et al., 2002).

It is important to observe that the viscous diffusion of vorticity was taken care of using the random walk method. In addition to the molecular diffusion, where necessary, the turbulent diffusion is accounted for by variation in the core radius.

4. Discussion and results

4.1. Isolated cylinder

To have an insight over the numerical results we first considered the flow around an isolated cylinder. This allows us to analyze its

consistency and define some numerical parameters, as for example, the number of panels used to define the cylinder. For this particular configuration, we used NP=300 source flat panels with constant density. The simulation was performed up to 1000 time steps with a value of $\Delta t=0.05$ for dimensionless time step. The time increment is given by $\Delta t=2\pi K/\text{NP}$, $0<K<1$ (Mustto et al., 1998).

The numerical analysis is conducted over a series of small discrete time steps Δt for each of which a discrete vortex element Γ_k is shed from circular cylinder surface element (panel). The intensity Γ_k of these newly generated vortices is determined using the no-slip condition (Eq. (4)). During each time every vortex element will move to ε-layer normal to the panels through a displacement $\varepsilon=\sigma_0=0.001d$ given by Ricci (2002).

The aerodynamic loads computations are evaluated between $t=30.0$ and 50.0 (Fig. 2). The results of the numerical simulation are presented in Table 1; the results of Blevins (1984) are experimental ones with 10% uncertainty and those of Mustto et al. (1998) are obtained using the vortex method associated with the Circle Theorem without turbulence model. The Strouhal number is defined as

$$S_t = \frac{fd}{U}, \tag{29}$$

where f is the detachment frequency of vortex.

The agreement between the present results and the experimental values is very good for the Strouhal number. The present drag coefficient shows a higher value as compared to the experimental result. The mean numerical lift coefficient, although very small, is not zero. The differences encountered are attributed mainly to the inherent three-dimensionality of the real flow for such a value of the Reynolds number ($\text{Re}=1.0 \times 10^5$), which is not
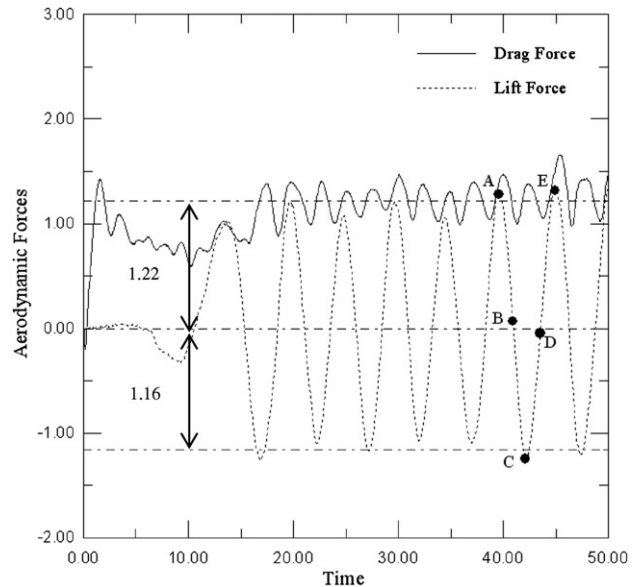

Fig. 2. Time history of drag and lift coefficients for an isolated circular cylinder.

Table 1
Mean lift and drag coefficients for an isolated circular cylinder.

Re = 1.0×10^5	$\overline{C}_D$	$\overline{C}_L$	$\overline{St}$	$\overline{A}_{C_L}$
Blevins (1984)	1.20	–	0.19	–
Mustto et al. (1998)	1.22	–	0.22	–
Present simulation	1.25	0.02	0.19	1.19

modeled in the simulation. On the other hand, the Strouhal number is insensitive to these three-dimensional effects.

Computed values for time-evolution drag and lift coefficients are plotted in Fig. 2. Fig. 3 shows plots of instantaneous pressure distributions on the cylinder surface. Pressure distributions A, B, C, D and E are related to instants A, B, C, D and E as indicated in Fig. 2. The vortex shedding effect can be seen in oscillations of the lift and drag coefficients. As soon as the numerical transient is over and the periodic steady state regime is reached (from $t=20$ on, approximately) the lift coefficient shows a mean variation between -1.16 and 1.22, approximately, with a dimensionless frequency (Strouhal number) about twice the frequency of the drag coefficient, in accordance to the physics involved in the flow. Fig. 2 indicates that the fluctuation of C_D has twice the frequency of C_L, because it fluctuates once for each of upper and lower shedding. For future discussions the mean amplitude of the lift coefficient curve is indicated by $\overline{A}_{C_L}$ and displayed in Table 1.

Instant A is defined by a maximum value of the lift coefficient; at this moment a large clockwise vortex structure (in fact a cluster of vortices) is detaching from the upper surface and moving toward the viscous wake; this structure is indicated in Fig. 4. As this structure moves downstream it pushes away an anti-clockwise structure that was stationed behind the cylinder and the drag coefficient increases.

At instant B the anti-clockwise structure detaches from the cylinder surface and is incorporated into the viscous wake; this process creates a low pressure region at the rear part of the cylinder which is associated to the high drag value (Figs. 3 and 5).

At this moment a new anti-clockwise vortex structure that has already started at the low side of the cylinder surface can be observed. The above described sequence of events repeats all over again. Therefore, the lowest value of the lift coefficient is observed when another cluster, now rotating in the anti-clockwise direction, leaves the body surface (point C in Figs. 3 and 6).

Gerrard (1966) has given an equivalent physical description of the mechanics of the vortex-formation region. A key factor in the

formation of a vortex-street wake is the mutual interaction between the two separating shear layers. It is postulated that a vortex continues to grow, fed by circulation from its connected shear
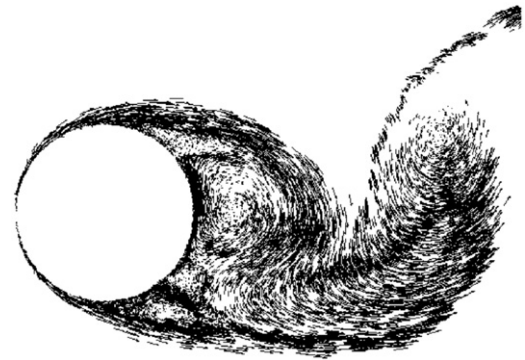

Fig. 4. Near wake behaviour for an isolated circular cylinder at an instant represented by point A.

Fig. 5. Near wake behaviour for an isolated circular cylinder at an instant represented by point B.
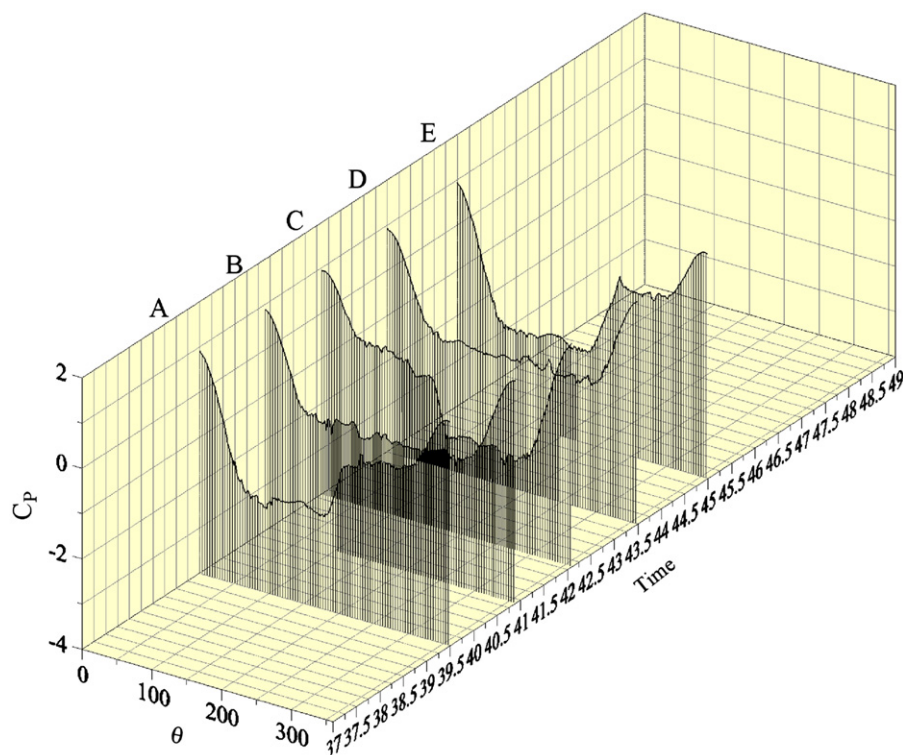

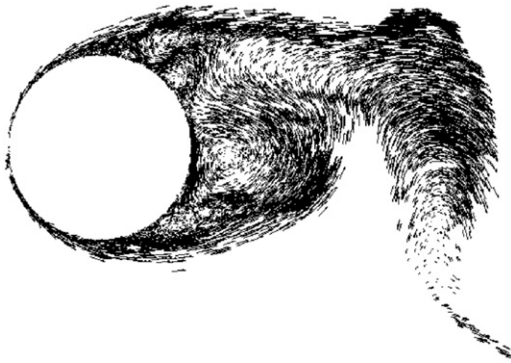Fig. 3. Instantaneous pressure distributions on the surface of an isolated circular cylinder.

Fig.6. Near wake behaviour for an isolated circular cylinder at an instant represented by point C.
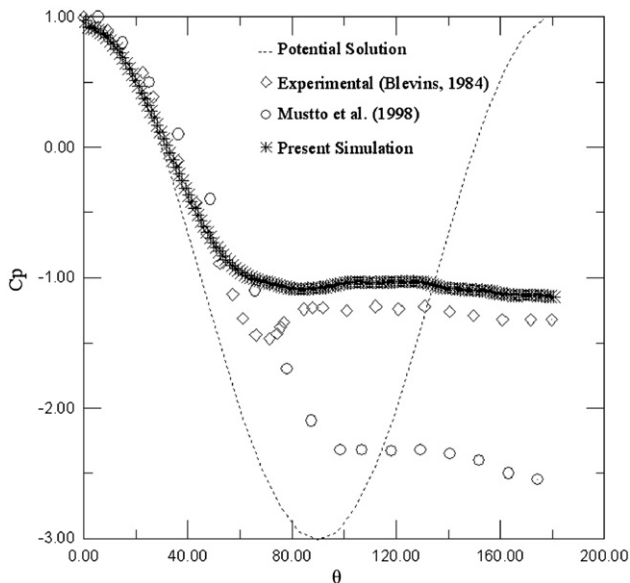

Fig. 7. Predicted pressure distributions for an isolated circular cylinder at $Re = 1.0 \times 10^5$.

layers, until it is strong enough to draw the opposing shear layers across the near wake. The approach of oppositely signed vorticity, in sufficient concentration, cuts off further supply of circulation to the growing vortex, which is then shed and moves off downstream.

Computed value of the mean pressure coefficient along the cylinder surface is compared with other results available in the literature. Fig. 7 shows the mean pressure distribution calculated for an isolated circular cylinder to be compared with the potential flow pressure distribution, the pressure distribution presented by Mustto et al. (1998) and the experimental values presented by Blevins (1984). The present result agrees very well with the experimental ones, except in a small neighborhood of $\theta \sim 78°$. From Fig. 7 one can observe that the predicted separation point occurs at around $\theta = 83°$, while the experimental value (Blevins, 1984) is around $\theta = 82°$. Another experimental investigation made by Son and Hanratty (1969) determined a value of $\theta = 78°$ for the separation angle. A very interesting observation was made by Achenbach (1968) for $Re = 1.0 \times 10^5$ (subcritical flow); it was found that the laminar boundary layer separates at $\theta = 78°$. Just before transition into the critical region at $Re = 2.6 \times 10^5$ the boundary layer is still laminar and separates at an angle $\theta = 94°$. Hence separation takes place in the laminar mode as experimentally expected for a subcritical Reynolds number forming free shear layer. An immediate transition to turbulence close to the cylinder is observed accompanied by a very short recirculation region.

4.2. Circular cylinder near a moving ground

To study the mechanisms of the ground effect a ground running at the speed of the freestream flow is used. In doing so no boundary layer develops on the ground surface to interfere with the body boundary layer and to modify the viscous wake. The key features of this flow are extensively discussed in the experimental work of Nishino (2007). Although the fundamental effects of the gap ratio (h/d) on the flow and force characteristics have been observed, the relation between destruction of the orderly Kármán vortex street and the significant drag reduction is still unclear .

For the numerical simulation we used the same 300 panels for the cylinder surface plus 300 panels to represent the moving ground. As already mentioned, no vorticity is generated on the ground surface, which avoids the development of a viscous boundary layer.

Table 2 presents values of the drag coefficient for circular cylinder placed at different values of the gap. One can easily observe three gap regimes given by Nishino (2007): large-gap ($h/d > 0.50$), intermediate-gap ($0.35 < h/d < 0.50$) and small-gap ($h/d < 0.35$) regimes.

Nishino (2007) measured the drag coefficient at two upper-subcritical Reynolds numbers (0.4×10^5 and 1.0×10^5); according to him an essentially two-dimensional flow around a cylinder with end-plates was observed, which was confirmed by analysing the surface oil flow patterns. Significant effects of the gap ratio were observed on the near wake structure and also on the time-averaged drag coefficient. For the large-gap regime, large-scale Kármán-type vortices were generated just behind the cylinder, resulting in higher drag coefficients of about 1.3. For the intermediate-gap regime, the Kármán-vortex shedding became intermittent, and hence the time-averaged drag coefficient decreased as h/d was reduced from 0.50 to 0.35. For the small-gap regime a dead fluid zone was created, bounded by two nearly parallel shear layers, each producing only small-scale vortices. For the cylinder without end-plates, on the other hand, no such significant effects of h/d were observed either on the near wake structure or on the drag coefficient.

Roshko et al. (1975) measured the time-averaged drag and lift coefficients for a circular cylinder placed near a fixed wall in a wind tunnel at $Re = 2.0 \times 10^4$, which lies in the upper-subcritical flow

Table 2
Summary of results for drag coefficient on the flow around a circular cylinder near a plane boundary.

h/d	Nishino (2007) without end-plates	Nishino (2007) with end-plates	Roshko et al. (1975)	Present simulation
0.00	–	–	0.795	–
0.05	0.965	–	0.857	1.199
0.10	0.958	–	–	1.154
0.15	0.952	–	0.954	1.305
0.20	0.939	–	–	1.441
0.25	0.933	–	1.029	1.451
0.30	0.930	–	–	1.366
0.35	0.931	–	–	–
0.40	0.922	–	1.136	1.398
0.45	0.926	1.311	–	1.389
0.50	0.924	1.323	–	1.371
0.60	0.920	1.373	1.281	1.390
0.80	0.899	1.385	–	1.341
0.90	–	–	1.266	–
1.00	0.881	1.375	–	1.307
1.50	0.854	1.337	–	1.283
1.80	–	–	1.243	–
2.00	0.845	1.304	–	1.246
3.00	–	–	1.234	–

regime, and showed that C_D rapidly decreased and C_L increased as the cylinder came close to the wall.

The column 5 of Table 2 shows the present numerical results for the time-averaged drag coefficient acting on a circular cylinder in moving ground. The aerodynamic forces computations are evaluated between $t=30$ and 50. The following analysis for the drag behaviour is based on Fig. 8(a).

The results from Nishino (2007) obtained with a running ground show that the drag acting on the cylinder without end-plates remains more or less constant. A cylinder with end-plates presents the same behaviour but at a higher value of the drag coefficient; it is worth to observe that in this situation, due to experimental difficulties, Nishino (2007) was not able to perform the tests for small-gap regime.

The results presented by Roshko et al. (1975) show that drag decreases as the gap ratio decreases, starting for the intermediate-gap regime; these results were obtained with a fixed ground.

The results from the present study obtained with a running ground show that the drag remains almost constant for the large and intermediate-gap regimes as predicted by the experiments of Nishino (2007); the values are a little higher, however. For the small-gap regime the drag decreases as the gap ratio decreases and, unfortunately, there are no experimental results to compare with.

Fig. 8(b) shows that the lift coefficient curve obtained numerically follows quite well the values obtained experimentally, except when $0.20 < h/d < 0.50$ where the calculated values are smaller. For smaller values of the gap ratio there are no experimental values available when the end-plates are added to the cylinder in the experiments from Nishino (2007). However, it is worth to observe that all the experimental and numerical results indicate the same limiting value for really small-gap.

Fig. 9 shows the instantaneous pressure distributions on the cylinder surface when the ground is moving; this sample refers to the gap ratio $h/d=0.45$. The pressure distributions A, B, C, D and E correspond to points A, B, C, D and E indicated in Fig. 10. At the instant represented by the point A one can clearly observe a low pressure distribution on the rear surface of the cylinder, leading to a maximum value of the drag curve; at the same time a high pressure distribution is found on the lower surface, which leads to a high lift value. The pressure distribution of instant B is almost

symmetrical with respect to the x-axis while maintaining low values at the rear part, thus explaining the almost zero value of the lift curve and a high value of the drag curve. Similar observations can be made about the pressure distributions and the lift and drag curves' behaviour at the other instants.

Some important features of the curves presented in Fig. 10 are

(i) The C_D curve oscillates at a frequency that is twice the frequency of the C_L curve.
(ii) Due to the proximity of the moving ground, the C_D curve presents a pair of small extreme values (small departure of the maximum and minimum values from the mean drag value) followed by a pair of large extreme values (large departure of the maximum and minimum values from the mean drag value).
(iii) As the gap ratio diminishes, the small extreme values become even smaller and eventually disappear. Therefore, the drag and lift curves oscillate at the same frequency.

Fig. 11 shows the near field flow pattern at instant A; at this instant we observe a maximum value of the C_L curve and a "small" maximum value of the C_D curve (Fig. 10). The analysis of the flow pattern at instant right before and after instant A shows that a cluster of vortices is moving on the upper side of the cylinder surface (leading to a high value of the lift) and pushes the anti-clockwise vortex structure toward the viscous wake; this vortex structure is deformed and somehow stretched by the presence of the nearby moving ground, leading to a "small" maximum value of the drag curve.

A similar analysis can be done for all the other instants identified in Fig. 10; the near field flow pattern for those instants is shown in Figs. 12–14. For instance, in Fig. 12 the near field flow pattern at instant B is depicted. At this instant a clockwise vortex structure is observed at the rear part of the cylinder surface; this vortex structure is also deformed by the action of the previous anti-clockwise structure that pulls it away from the body surface. This configuration is one, responsible for a "small" minimum value of the C_D curve, and an almost zero value for the C_L curve. Figs. 13 and 14 are associated to instants C and D at which the extreme
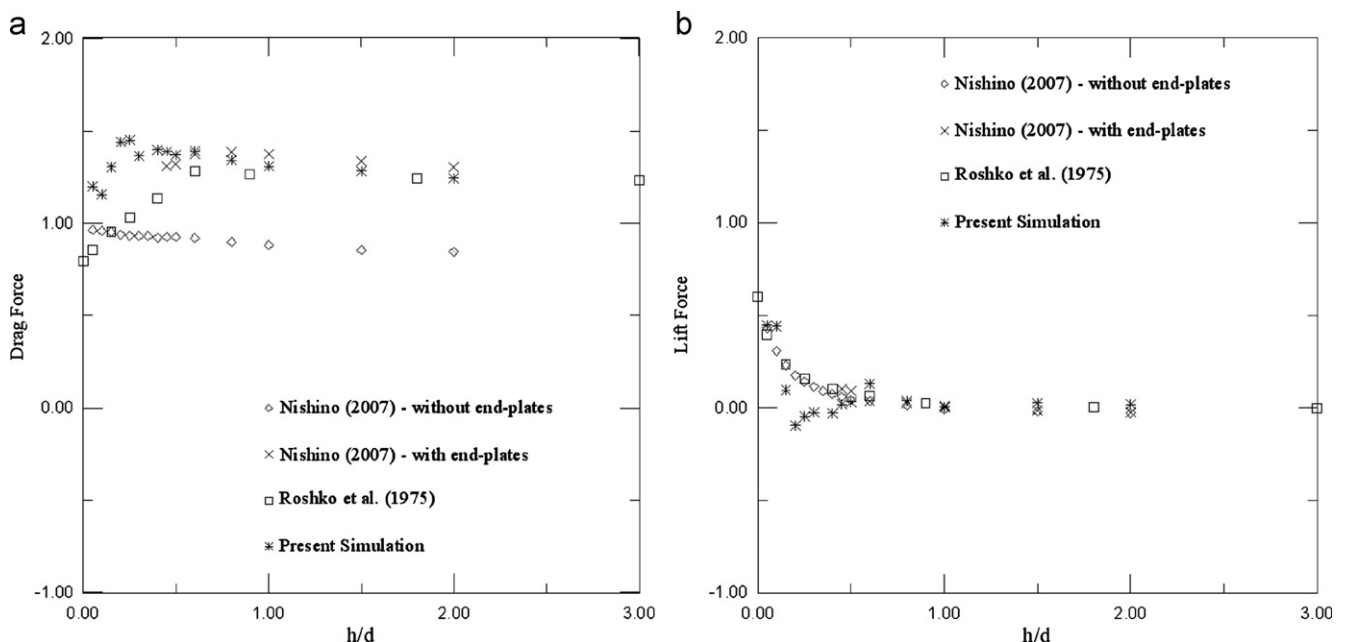

Fig. 8. Time-averaged drag and lift coefficients vs. gap ratio for different end conditions: (a) drag force and (b) lift force.
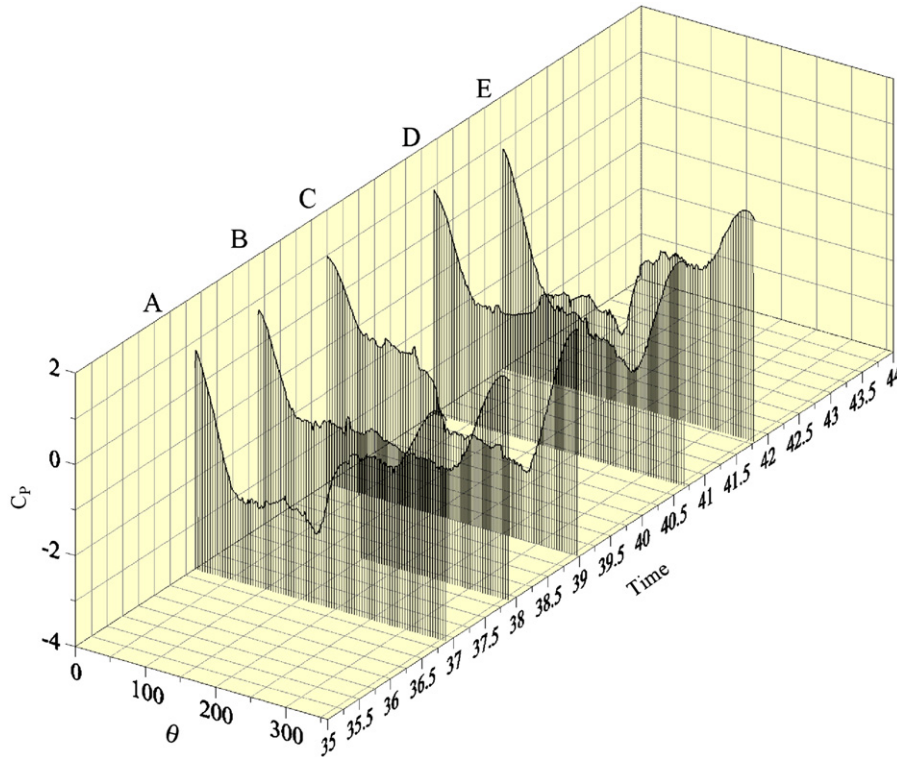
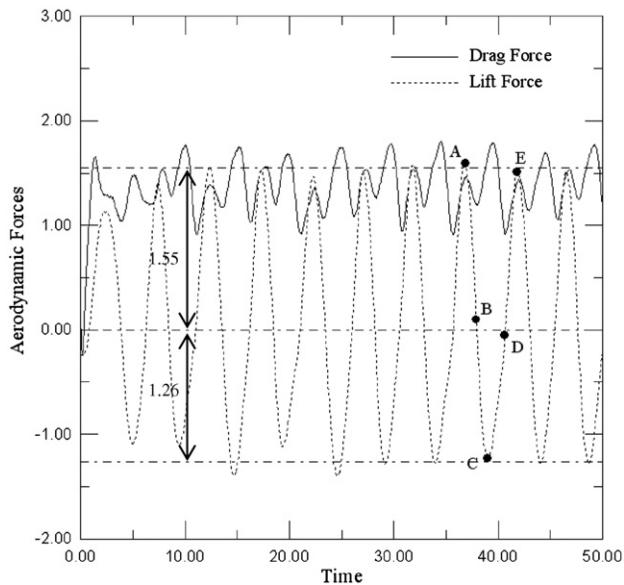Fig. 9. Instantaneous pressure distribution on the surface of a circular cylinder using moving ground for $h/d=0.45$.

Fig. 10. Time history of drag and lift for a circular cylinder using moving ground for $h/d=0.45$.

Fig. 11. Near wake behaviour using moving ground at an instant represented by point A for $h/d=0.45$.

values of the C_D are "large", observing that the near field vortex structure does not deform.

Fig. 15 shows the time variation of the drag and lift coefficients for the gap ratio $h/d=0.05$. From this figure one can observe the tendency to the cessation of the periodic vortex shedding due to the presence of a plane wall placed in the close vicinity of the cylinder. The variation of the Strouhal number with the gap ratio is presented in Table 3; it is clear that the Strouhal number decreases as the gap ratio decreases, with the maximum decrease of about 50%. This decrease agrees with the fast decay of the *time-averaged* drag coefficient in experiments from Nishino (2007).
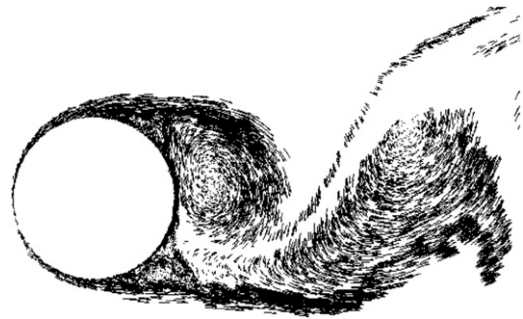
Fig. 16 is associated to instant C in which the extreme value of the C_D curve is high and Fig. 17 shows plots of instantaneous pressure distributions on the cylinder surface. It is clear at instant C from Fig. 17 that the pressure distribution generates a downward force, which tends to push the cylinder toward the wall boundary. The numerical result for the gap ratio $h/d=0.05$ suggests that the drag reduction of a circular cylinder in ground effect is directly related to the cessation of the Kármán vortex shedding. Further investigations are required, however, to fully resolve this issue.

Fig. 18 shows the position of the wake vortices for the gap ratio $h/d \rightarrow \infty$ at the last step of the computation ($t=50$) where we can clearly observe formation and shedding of large eddies in the wake. We can also visualize the vortex pairing process, where the vortices rotate in opposite directions and are connected to each other by a vortex sheet. The rightmost part of the wake corresponds to the numerical transient that occurs before a periodic steady state regime is reached. Finally, for a not so small gap (Fig. 19), the wake seems to be formed by a series of "mushroom" type vortex structure, which will be destroyed far away by the moving ground.

Fig. 12. Near wake behaviour using moving ground at an instant represented by point B for $h/d = 0.45$.
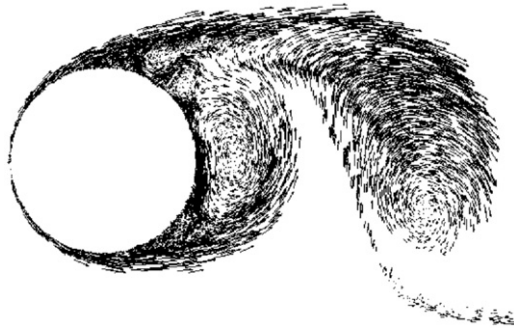

Fig. 13. Near wake behaviour using moving ground at an instant represented by point C for $h/d = 0.45$.
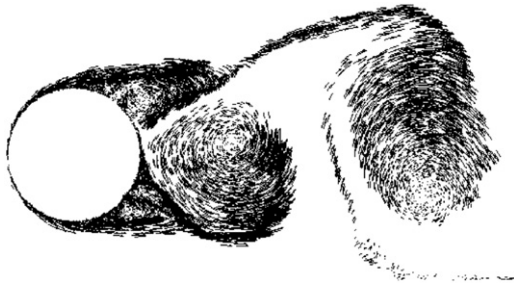

Fig. 14. Near wake behaviour using moving ground at an instant represented by point D for $h/d = 0.45$.

Therefore, the moving plane has significant effect on the vortex shedding.

Further investigations are necessary to fully understand the drag behaviour as well as the interaction between boundary layers when the gap is very narrow in comparison with the cylinder diameter: Fig. 20 gives us some hints.

5. Conclusions

In this study of vortex shedding, destruction of the vortex street and drag reduction of a circular cylinder near a moving ground have employed a numerical Lagrangian technique, called the vortex method. All the simulations are carried out with a high value of the Reynolds number of 1.0×10^5 using turbulence modeling. The present numerical results are in good agreement with the limited amount of experimental data available in the literature. The use of global and local quantities combined to the near field flow pattern observations can be used to understand the complex mechanisms that lead to the origin and the time evolution of the aerodynamic loads. The instantaneous pressure distribution on the cylinder
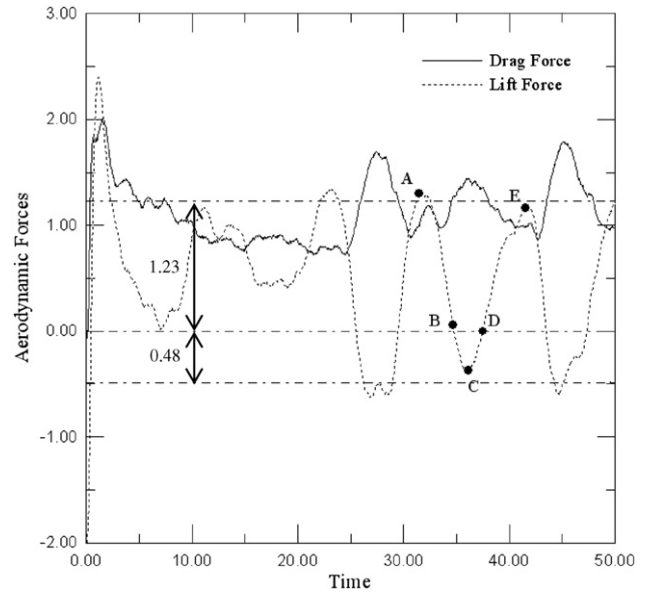

Fig. 15. Time history of drag and lift for a circular cylinder using moving ground for $h/d = 0.05$.

Table 3
Present simulation: Strouhal number for different distances between the circular cylinder and the plane boundary.

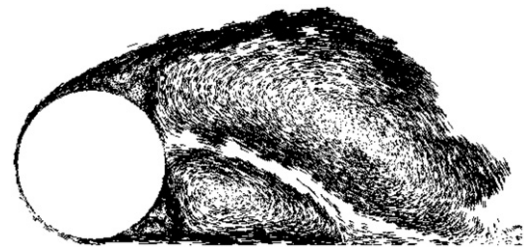| h/d	$\overline{St}$
0.05	0.10
0.10	0.13
0.15	0.16
0.20	0.17
0.25	0.20
0.30	0.20
0.40	0.20
0.45	0.20
0.50	0.20
0.60	0.20
0.80	0.20
1.00	0.21
1.50	0.21
2.00	0.21

Fig. 16. Near wake behaviour using moving ground at an instant represented by point C for $h/d = 0.05$.

surface allows one to follows, in time, its evolution. This feature can be of importance when the body is oscillating near a ground plane and in many other situations of practical interest. It becomes obvious that one has a powerful tool if the time evolution of the pressure distribution is analyzed simultaneously with the integrated loads (lift and drag).

As already used in the experimental work dealing with the aerodynamic of high speed racing cars, the moving ground model used in the numerical simulations (although with a simple
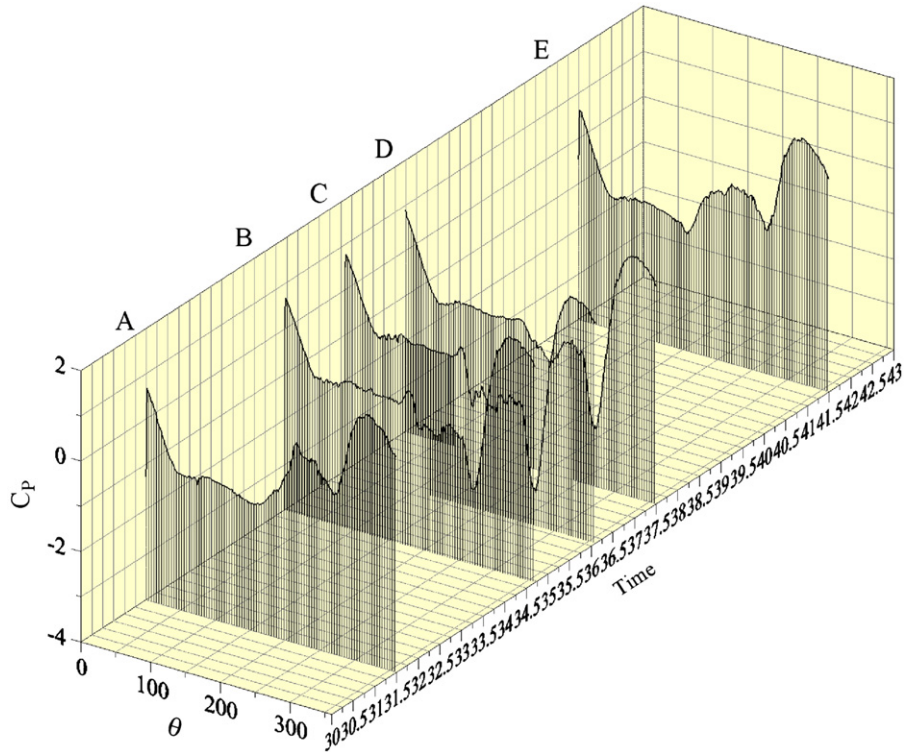
Fig. 17. Instantaneous pressure distribution on the surface of a circular cylinder using moving ground for $h/d=0.05$.

Fig. 18. Final position of the vortices for the flow past an isolated circular cylinder at Reynolds number of 1.0×10^5.

Fig. 19. Final position of the vortices for the flow past a circular cylinder in moving ground for $h/d=0.45$ at Reynolds number of 1.0×10^5.

Fig. 20. Final position of the vortices for the flow past a circular cylinder in moving ground for $h/d=0.05$ at Reynolds number of 1.0×10^5.

geometrical form body) is able to predict the main features of the flow around a body in close proximity of a flat surface. The methodology developed in this paper is greatly simplified by the utilization of the vortex method.

Acknowledgments

References

Achenbach, E., 1968. Distribution of local pressure and skin friction around a circular cylinder in cross-flow up to Re=5.0×10^6. J. Fluid Mech. 34 (4), 625–639.

Alcântara Pereira, L.A., Ricci, J.E.R., Hirata, M.H., Silveira Neto, A., 2002. Simulation of Vortex shedding flow about a circular cylinder with turbulence modeling. CFD J. 11 (3), 315–322.

Alcântara Pereira, L.A., Hirata, M.H., Manzanares Filho, N., 2004. Wake and aerodynamics loads in multiple bodies—application to turbomachinery blade rows. J. Wind Eng. Ind. Aerodyn. 92, 477–491.

Batchelor, G.K., 1953. The Theory of Homogeneous Turbulence. Cambridge University Press, Cambridge, England, UK.

Bearman, P.W., Zdravkovich, M.M., 1978. Flow around a circular cylinder near a plane boundary. J. Fluid Mech. 89, 33–47.

Blevins, R.D., 1984. Applied Fluid Dynamics Handbook. Van Nostrand Reinhold Co.

Chorin, A.J., 1973. Numerical study of slightly viscous flow. J. Fluid Mech. 57, 785–796.

Gerrard, J.H., 1966. The mechanics of the formation region of vortices behind bluff bodies. J. Fluid Mech. 25, 401–413.

Grass, A.J., Raven, P.W.J., Stuart, R.J., Bray, J.A., 1984. Influence of boundary layer velocity gradients and bed proximity on vortex shedding from free spanning pipelines. Trans. ASME J. Energy Resour. Technol. 106, 70–78.

Hirata, M.H., Alcântara Pereira, L.A., Recicar, J.N., Moura, W.H., 2008. High Reynolds number oscillations of a circular cylinder. J. Braz. Soc. Mech. Sci. & Eng. XXX (4), 300–308.

Kamemoto, K., 1993. Procedure to estimate unsteady pressure distribution for vortex method (in Japanese). Trans. Jpn. Soc. Mech. Eng. 59 (568 B), 3708–3713.

Kamemoto, K., 2004. On contribution of advanced vortex element methods toward virtual reality of unsteady vortical flows in the new generation of CFD. J. Braz. Soc. Mech. Sci & Eng. 26 (4) Rio de Janeiro, Oct./Dec.

Katz, J., Plotkin, A., 1991. Low Speed Aerodynamics: From Wing Theory to Panel Methods. McGraw Hill, Inc.

Lei, C., Cheng, L., Kavanagh, K., 1999. Re-examination of the effect of a plane boundary on force and vortex shedding of a circular cylinder. J. Wind Eng. Ind. Aerodyn. 80, 263–286.

Leonard, A., 1980. Vortex methods for flow simulation. J. Comp. Phys. 37, 289–335.

Lesieur, M., Métais, O., 1996. New trends in large eddy simulation of turbulence. A Rev. Fluid Mech. 28, 45–82.

Lin, C., Lin, W.J., Lin, S.S., 2005. Flow characteristics around a circular cylinder near a plane boundary. In: Proceedings of the Sixteenth International Symposium on Transport Phenomena (ISTP-16), 29 August–1 September, Prague, Czech Republic, (CD-ROOM).

Métais, O., Lesieur, M., 1992. Spectral Large eddy simulations of isotropic and stably-stratified turbulence. J. Fluid Mech. 239, 157–194.

Mustto, A.A., Hirata, M.H., Bodstein, G.C.R., 1998. Discrete vortex method simulation of the flow around a circular cylinder with and without rotation. In: A.I.A.A. Paper 98-2409, Proceedings of the 16th A.I.A.A. Applied Aerodynamics Conference, Albuquerque, NM, USA,.

Nishino, T., 2007. Dynamics and stability of flow past a circular cylinder in ground effect. Ph.D. Thesis, Faculty of Engineering Science and Mathematics, University of Southampton.

Ricci, J.E.R., 2002. Numerical simulation of the flow around a body in the vicinity of a plane using vortex method. Ph.D. Thesis, Mechanical Engineering Institute, UNIFEI, Itajubá, MG, Brazil (in Portuguese).

Roshko, A., Steinolfson, A., Chattoorgoon, V., 1975. Flow forces on a cylinder near a wall or near another cylinder. In: Proceedings of the 2nd US Nation Conference on Wind Engineering Research, Fort Collins, Paper IV-15.

Sarpkaya, T., 1989. Computational methods with vortices—the 1988 freeman scholar lecture. J. Fluids Eng. 111, 5–52.

Shintani, M., Akamatsu, T., 1994. Investigation of two-dimensional discrete vortex method with viscous diffusion model. CFD J. 3 (2), 237–254.

Smagorinsky, J., 1963. General circulation experiments with the primitive equations. Mon. Weather Rev. 91 (3), 99–164.

Son, J.S., Hanratty, T.J., 1969. Velocity gradients at the wall for flow around a cylinder at Reynolds number from 5.0×10^3 to 1.0×10^5. J. Fluid Mech. 35 (2), 353–368.

Stock, M.J., 2007. Summary of vortex methods literature (a lifting document rife with opnion). April, 18: © 2002–2007 Mark J. Stock.

Taneda, S., 1965. Experimental investigation of vortex streets. J. Phys. Soc. Jpn. 20, 1714–1721.

Uhlman, J.S., 1992. An Integral Equation Formulation of the Equation of an Incompressible Fluid. Naval Undersea Warfare Center T.R. 10-086.

Zdravkovich, M.M., 1985a. Observation of vortex shedding behind a towed near a wall. In: Flow Visualization III: Proceedings of the Third International Symposium on Flow Visualization, W.J. Yang (Ed.). Hemisphere, Washington DC, pp. 423–427.

Zdravkovich, M.M., 1985b. Forces on a circular cylinder near a plane wall. Appl. Ocean Res. 7, 197–201.

Zdravkovich, M.M., 2003. Flow around Circular Cylinders. Vol. 2: Applications. Oxford University Press, Oxford, UK.